Sulfide oxide XZnSO (X = Ca or Sr) as novel active photocatalytic water splitting solar-to-hydrogen energy conversion

A.H. Reshak

New Technologies – Research Centre, University of West Bohemia, Univerzitni 8, 306 14 Pilsen, Czech Republic

ARTICLE INFO

ABSTRACT

The photocatalytic, structural and transport properties of the newly synthesized sulfide oxide CaZnSO and SrZnSO compounds are comprehensively investigated by means of first and second-principles calculation in order to explain the semiconductor's 'photo-excitation' state mechanism in CaZnSO and SrZnSO. At the same time, the influence of the substitution of Ca^{2+} by Sr^{2+} on the structural properties and, hence, on the photo-catalytic properties, are investigated. The optical conductivity and the absorption level exhibit an obvious enhancement from the ultraviolet to the visible light region when we move from Ca to Sr. This shows that the absorption edge moves from $\lambda = 387.4 \rightarrow \lambda = 442.7$ nm, which corresponds to the direct optical band gap of 3.2 eV $\rightarrow 2.8$ eV, which is well matched with the solar spectrum and the sufficient negative conduction band potential for reduction of H^+/H_2. The calculated electronic band structure and the angular momentum character of various structures confirm that CaZnSO and SrZnSO possess a direct fundamental energy band gap of about 3.7 eV (CaZnSO) $\rightarrow 3.1$ eV (SrZnSO), and the electronic charge distribution reveals a clear map of the electronic charge transfer and the chemical bonding. Furthermore, the carrier concentration (n) as a function of chemical potential at three constant temperatures (T) and n as a function of T at fixed chemical potential were calculated. It was found that n increases exponentially with increasing T and reveals that the CaZnSO and SrZnSO are p-type semiconductors. Based on these results, one can conclude that CaZnSO and SrZnSO satisfied all requirements to be an efficient photocatalyst. This will greatly improve the search efficiency and greatly help experiments to save resources in the exploration of new photocatalysts with good photocatalytic performance.

1. Introduction

Due to control of the electronic communication between the oxide and chalcogenide layers in a transition metal, the layered oxychalcogenides exhibit novel and unusual properties which is not possible to access in the oxides or chalcogenides [1]. The ordering of two anions in the crystal results in a layered crystal structure, which causes significant influence on the electronic properties [2,3]. It has been reported that the local electric polarity of CoS_3O, FeS_3O and ZnS_3O tetrahedra which was observed in transition metal oxychalcogenides CaCoSO, CaFeSO and CaZnSO, respectively, can influence the linear and nonlinear optical properties and the magnetic properties [3–6]. Recently, Sambrook et al. [3], have synthesized pure CaZnSO in a non-centrosymmetric hexagonal space group (P63mc) with two formula per unit cell. They reported that lattice constants are **a** = 3.75726(3) Å and **c** = 11.4013(1) Å, and that replacing Ca^{2+} with Sr^{2+} in CaZnSO causes the introduction of a different chemical pressure which in turn influences the polarity of the crystal structure, energy band gap and hence the optical properties. At the same time, they asserted that it is not

possible to synthesize SrZnSO [3]. Very recently, Liu et al. [2] succeeded in synthesizing a novel polar SrZnSO in a non-centrosymmetric hexagonal space group (P63mc) with lattice constants a = 3.90442(6) Å and c = 11.6192(2) Å. They found that the SrZnSO is isostructural to CaZnSO, but is less polar than CaZnSO. They described the structural properties of SrZnSO. Therefore, as a natural extension to the work of Liu et al. and Sambrook et al., we have addressed ourselves to investigating the electronic band structure, density of states, electronic charge density distribution, photophysical and photocatalytic properties and thermoelectric properties of SrZnSO and CaZnSO using the first and second-principles methods. It has been reported that ZnS [7–11] and ZnO [12–17] are promising photocatalytic H_2 production materials under visible light irradiation. Therefore, we have addressed ourselves to investigating the photocatalytic performance of SrZnSO and CaZnSO as ZnS and ZnO-containing materials. It is well known that ZnS and ZnO generate electron-hole pairs by photoexcitation immediately and their extraordinary photostability is due to the highly negative reduction potentials of those excited electrons.

In recent years, due to the improvement of computational

E-mail address: maalidph@yahoo.co.uk.

technologies, it has been proven that the first-principles calculation is a strong and useful tool to predict the crystal structure and properties related to the electron configuration of a material before its synthesis [18–26]. It is well known that the DFT approaches have the ability to accurately predict the ground state properties of the materials, and the developed analysis tools are vital to investigating their intrinsic mechanism. It is anticipated that first-principle material approaches will greatly improve the search efficiency and greatly help experiments aimed at saving resources in the exploration of new materials with good performance [18–26]. For instance, several researchers have used the DFT calculation for exploration of new photocatalysts and found good agreement with experimental results [27–33]. We would like to mention that, in our previous work [34–37], we have calculated the photocatalytic properties and the energy band gaps using the full-potential method for several systems whose photocatalytic and energy band gaps are known experimentally, and a very good agreement with the experimental data was obtained. Thus, we believe that our calculations reported in this paper will produce very accurate and reliable results. The aim of this work is to focus on the photocatalytic activity of non-centro-symmetric CaZnSO and SrZnSO as new, green and efficient photocatalysts.

2. Structural aspects and methodology

The crystal structure of CaZnSO (SrZnSO) has polar layers in the *ab*
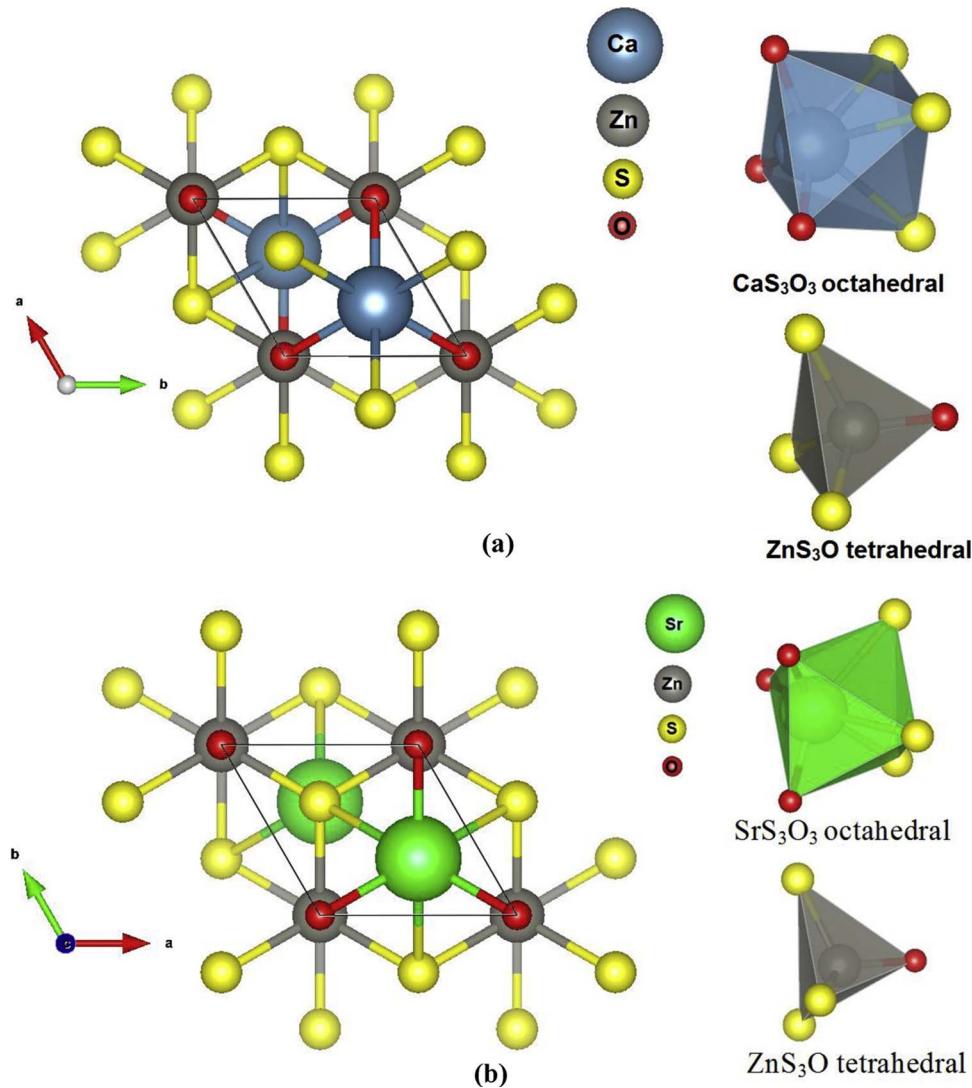
plane of S atom-vertex-sharing ZnS_3O tetrahedral that are separated by Ca (Sr) ions of the (CaS_3O_3) (SrS_3O_3) octahedral [2], see Fig. 1. Sambrook et al. [3] reported that the substitution of Ca^{2+} (radii = 180 pm) by larger Sr^{2+} (radii = 200 pm) in CaZnSO introduces a different chemical pressure, which can change the structural polarity and reduce the fundamental energy band gap from 3.7 eV [3] to 3.1 eV [2], resulting in enhancing the optical activity. Therefore, to investigate the suitability of CaZnSO and SrZnSO for use as active photocatalysts, *ab initio* first-principle calculations are performed utilizing the full-potential method (wien2k code [38]) within the generalized gradient approximation (PBE-GGA) [39] to optimize the experimental lattice constant and the experimental atomic positions [2]. The lattice constants and the atomic positions obtained are listed in Table S1 and S2 (supplementary materials) in comparison with the available experimental data [2,3]. The recently modified Becke-Johnson potential (mBJ) [40] is used to calculate the ground state properties. The thermoelectric properties of CaZnSO and SrZnSO are obtained from the ground state within the limits of Boltzmann theory [41–43] and the constant relaxation time approximation as implemented in the Boltz-TraP code [44].

In order to achieve energy eigenvalue convergence, the wave functions in the interstitial region are expanded using plane waves with a cutoff of $R_{MT} \times K_{max} = 7.0$, where K_{max} is the plane wave cut-off, and R_{MT} is the smallest of all atomic sphere radii. The charge density was Fourier expanded up to $G_{max} = 12(a.u.)^{-1}$. The maximum l value for


Fig 1. (a, b) Crystal structure of CaZnSO and SrZnSO; The crystal structure of CaZnSO (SrZnSO) has polar layers in the *ab* plane of S atom-vertex sharing ZnS_3O tetrahedral that are separated by Ca (Sr) ions of the (CaS_3O_3) (SrS_3O_3) octahedral.
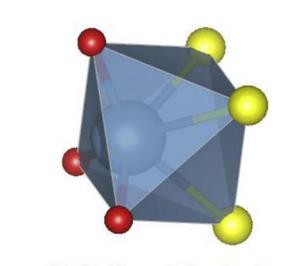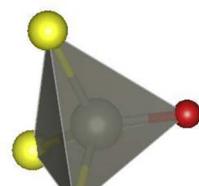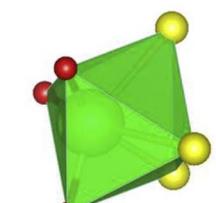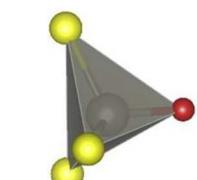
the wave function expansion inside the atomic spheres was confined to $l_{max} = 10$. Self-consistency is obtained using 4000 $\vec{k}$ points in the irreducible Brillouin zone (IBZ). The self-consistent calculations are converged since the total energy of the system is stable within 0.00001 Ry. The electronic properties are calculated using 50000 $\vec{k}$ points in the IBZ. The input required for calculating the total and partial density of states (DOS) are the energy eigenvalues and eigenfunctions which are the natural outputs of a band structure calculation. Therefore, from the band structure calculation the DOS are calculated by means of the modified tetrahedron method [45].

3. Results obtained and discussion of details

Since CaZnSO and SrZnSO crystallize in a non-centro-symmetric structure, it is very interesting to highlight that the non-centro-symmetric structure induces a spontaneous polarization due to the displacement of the center of the positive and negative charges in a unit cell [46]. Due to the fact that their positive and negative charges have different centers of symmetry, the non-centro-symmetric materials are among the ferroelectric materials that have a macroscopic polarization which induces the accumulation of charges at the surfaces [47]. Thus, a spontaneous polarization can be screened by free electrons (e^-) in the conduction band (CB) and free holes (h^+) in the valence band (VB), and/or by ions adsorbed on the surface from the solution forming a Stern layer [48]. A positive charge in positive fields is screened by internal and external mechanisms [49]. The internal mechanism forms a negatively charged region below the surface, and the external mechanism consists of the adsorption of foreign negatively charged ions at the surface. In contrast, the opposite reactions take place in negative fields, and the adsorbed foreign ions are positively charged. This charge reallocation generates an electric field around the charge region [50]. A polarization field is compensated for at equilibrium by the screening mechanisms. Therefore, the photogenerated electrons can easily migrate to the surface and give rise to oxidation and reduction products at different locations [51]. This in turn enhances the photocatalytic activity. We should emphasize that the unique photochemistry of the non-centrosymmetric materials may be utilized to launch some new photoreaction pathways. The Zn–O, Zn–S, Ca(Sr)–S and Ca(Sr)–S units possess strong electron cloud overlap and prefer to attract h^+ and repel e^-, thus facilitating separation of the photogenerated e^-–h^+ pairs. This in turn enhances the photocatalytic activity. It is interesting to highlight that the polarizability cause to lower the potential energy of charged particles and transition states regardless of whether these particles are negatively or positively charged [52].

For photocatalytic water splitting, the optical band gap of the photocatalyst material must be sufficiently large to overcome the endothermic character of the water-splitting reaction, i.e. larger than 1.23 eV [53]. The other important factor for a photocatalyst is the range of light absorbed; the optical absorption induces the transfer of e^- from the VB to CB, generating the e^-–h^+ pairs which can thence migrate to the surface to participate in oxidation and reduction reactions, respectively [53,54]. The appropriate band gap width and suitable conduction band edge position together contribute to the optimal H2 production activity under light irradiation. Therefore, we calculated the absorption spectrum (Fig. 2a,b) in order to estimate the optical energy band gap value. The optical energy band gap ($E_{g(optical)}$) can be obtained as follows: the square of the absorption coefficient, $[I(\omega)]^2$, is linear with energy (E) for direct optical transitions in the absorption edge region, whereas the square root of the $I(\omega)$ is linear with E for indirect transitions [27,28]. Data plots of CaZnSO and SrZnSO for $[I(\omega)]^2$ vs. E in the absorption edge region are shown in the inset of Fig. 2a and 2b, which show that the $[I(\omega)]^2$ vs. E plot is nearly linear. These features suggest that the absorption edges of CaZnSO and SrZnSO are caused by direct transitions. The absorption level of CaZnSO and SrZnSO exhibited an obvious enhancement from the ultraviolet to the visible light

region when we move from Ca to Sr. This shows that the absorption edge moves from $\lambda = 387.4 \rightarrow \lambda = 442.7$ nm, which corresponds to the direct optical band gap of 3.2 eV $\rightarrow$ 2.8 eV, which is well matched with the solar spectrum and the sufficient negative conduction band potential for reduction of H^+/H_2 [55–57]. Therefore, CaZnSO can be used in active photocatalytic water splitting solar-to-hydrogen energy conversion in the UV light region, while SrZnSO can be used in the visible light region. When a photocatalyst absorbs radiation from sunlight, it produces electron and hole pairs. The electrons of the valence band becomes excited when illuminated by light. The excess energy of this excited electron promotes the electron to the conduction band, thereby creating an e^- and h^+ pair (Fig. 2c).

Usually, the locations of the top of the VB (TVB) and bottom of the CB (BCB) determine the oxidation and reduction capabilities of photogenerated h^+ and e^-, respectively [58]. The reduction potential level of the electron-accepters should be energetically below the BCB, whereas the oxidization potential level of the electron-donors should be above the TVB [59]. The photocatalytic oxidation of the materials is mainly attributed to the participation of superoxide radicals ($O_2 \cdot ^-$), hydroxyl radicals ($\cdot$OH) and photogenerated holes [60], see Fig. 2c and d. In order to understand the photocatalytic mechanism in XZnSO, the reduction and oxidation potentials of the CB and VB edges at the point of zero charge can be calculated following the equations given in Ref. 61:

$$E_{CB} = \chi - E^C - (E_g/2) \tag{1}$$

$$E_{VB} = E_{CB} + E_g, \tag{2}$$

where E_{CB} and E_{VB}, respectively, are the potentials of CB and VB edges, E^C is the free energy corresponding to the hydrogen scale, and the value is ~ 4.5 eV [61], E_g and χ are the band gap and the electronegativity of semiconductors, respectively. The χ is defined as the geometric mean of the absolute electronegativities of the constituent atoms. The absolute electronegativity of an individual atom is the arithmetic mean of the atomic electron affinity and the first ionization energy [61]. The E_{CB} and E_{VB} values of the CaZnSO and SrZnSO are shown in Fig. 2d. It can be clearly seen that the CB edge potential of CaZnSO is more negative than that of SrZnSO, indicating that the CaZnSO has stronger reduction power for H_2 production than the SrZnSO. A semiconductor with a more negative CB edge potential has stronger reduction power for the H_2 production from water [61]. Generally, an appropriate band gap width and suitable CB edge position together contribute to the optimal H_2 production activity under light irradiation. Therefore, a balance between the light absorption capacity and the reduction power in the investigated materials leads to a higher efficiency of light-driven photocatalytic H_2 production. This stage is referred to as the semiconductor's 'photo-excitation' state. To explain this mechanism in CaZnSO and SrZnSO, we calculated the optical conductivity ($\sigma(\omega) = \frac{4\pi k(\omega)}{\lambda}$), which is directly related to the energy band structure of solids [62], and deep insight into the electronic structure of the materials can be further obtained from the optical conductivity. Furthermore, from the imaginary part of the optical conductivity, the values of the plasma energy can be obtained: these are $\hbar\omega_p^\perp(\omega) = 7.850$ eV and $\hbar\omega_p^{II}(\omega) = 8.830$ eV. The calculated optical conductivity (Fig. 3(a, b)), depicts the conduction induced by the electrons which move from valence band to the conduction band upon absorption of incident light. Since the optical conductivity appears as a result of absorption, the features of the curves in Fig. 2(a, b) and Fig. 3(a, b) are closely related and the peaks represent optically induced electronic transitions between different states of the occupied valence band and the unoccupied conduction band.

In further investigation, we calculated the electronic electrical conductivity as shown in Fig. 3(c, d). In general, the electronic electrical conductivity ($\sigma = ne\eta$) is related to the density of charge carriers (n) and their mobility ($\eta = e\tau/m^*$), where η represents the mobility, e the charge of carriers, τ the relaxation time and m^* the effective mass. It
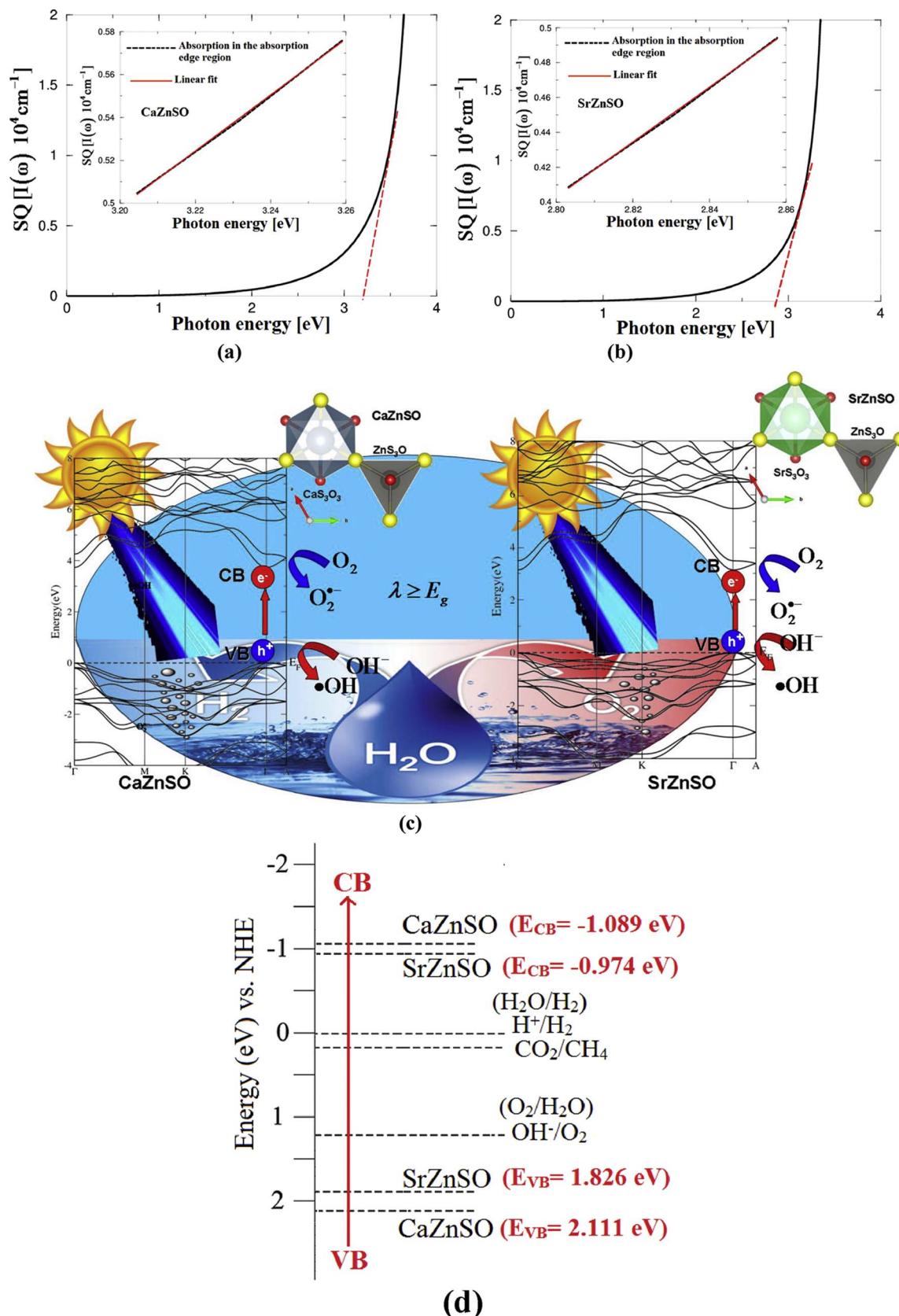
Fig. 2. (a, b) Data plots of CaZnSO and SrZnSO for $[I(\omega)]^2$ versus energy in the absorption edge region are shown in the inset of Fig. 2a and b, which show that the $[I(\omega)]^2$ versus energy plot is nearly linear. These features suggest that the absorption edges of CaZnSO and SrZnSO are caused by direct transitions. The absorption level of (CaZnSO) SrZnSO exhibited an obvious enhancement from ultraviolet to visible light region when we move from Ca to Sr, it shows the absorption edge moves from $\lambda = 387.4 \rightarrow \lambda = 442.7$ nm, which corresponds to the direct optical band gap of 3.2 eV $\rightarrow 2.8$ eV, that is well matched with solar spectrum and the sufficient negative conduction band potential for reduction of H^+/H_2; (c) Schematic diagrams of charge transfer and photocatalytic mechanism of CaZnSO and SrZnSO; When photocatalyst absorbs radiation from sunlight, it produces electron and hole pairs. The electron of the valence band becomes excited when illuminated by light. The excess energy of this excited electron promoted the electron to the conduction band therefore, creating the negative electron (e^-) and positive hole (h^+) pair. This stage is referred as the semiconductor's 'photo-excitation' state; (d) The schematic diagrams of potential in eV vs. NHE for CaZnSO and
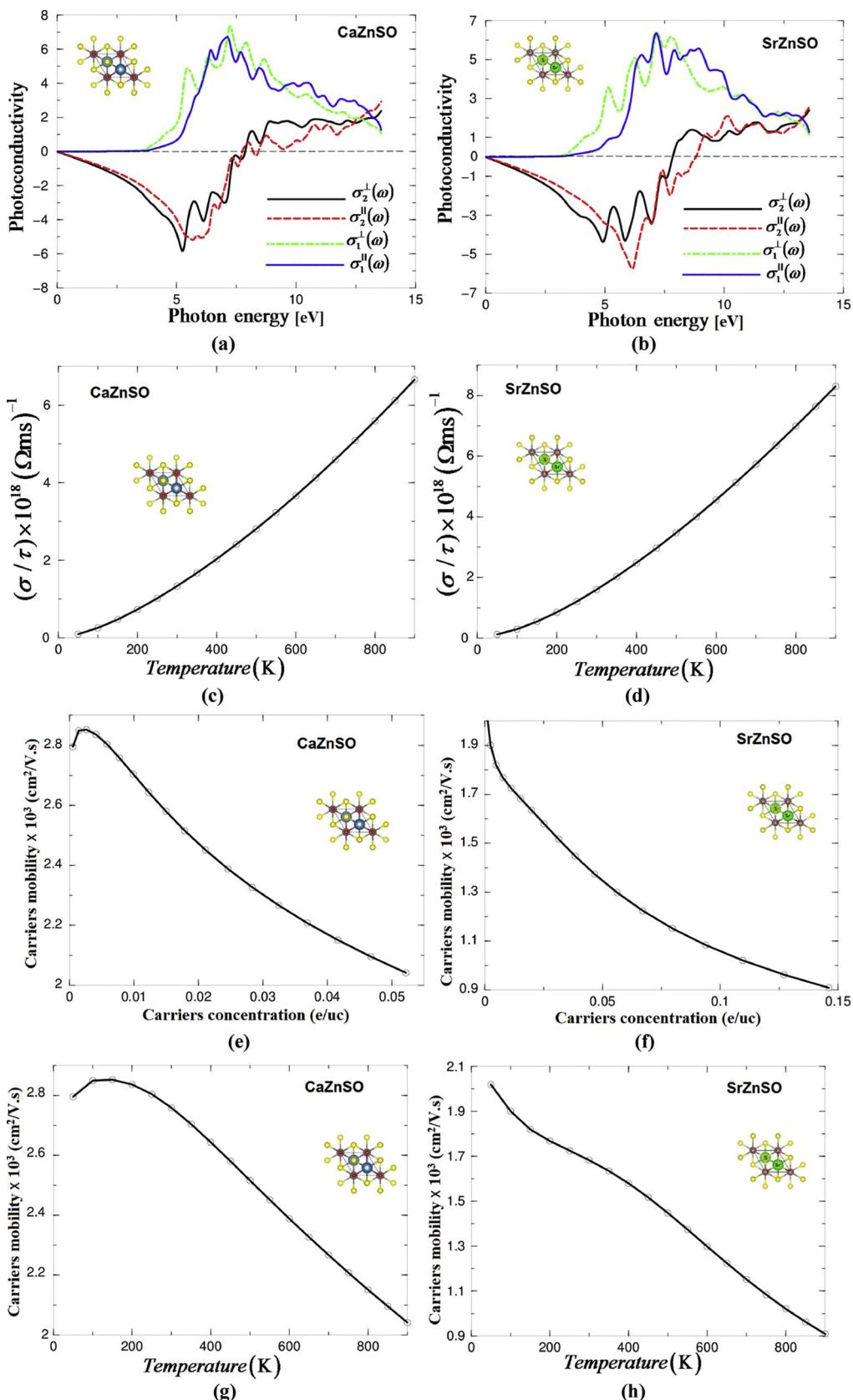
Fig. 3. (a, b) The calculated optical conductivity; (c, d) the calculated electronic electrical conductivity; (e, f) shows the carrierś mobility as a function of carrier concentration (*n*), which clearly shows a significant reduction in the carrierś mobility with an increase in the carrier concentration due to increasing the scattering; (g, h) the carrierś mobility as a function of temperature. It clearly shows a significant reduction in the carrierś mobility with an increase in the temperature, which is attributed to the fact that raising the temperature causes the vibration to increase, and hence, the mobility, resulting in an increase in the scattering which leads to suppression of the mobility; (i, j) The carrier concentration as function of chemical potential *μ–E_F* at room temperature and other two randomly selected temperatures; (k, l) The carrier concentration as a function of temperatures at fixed chemical potential.
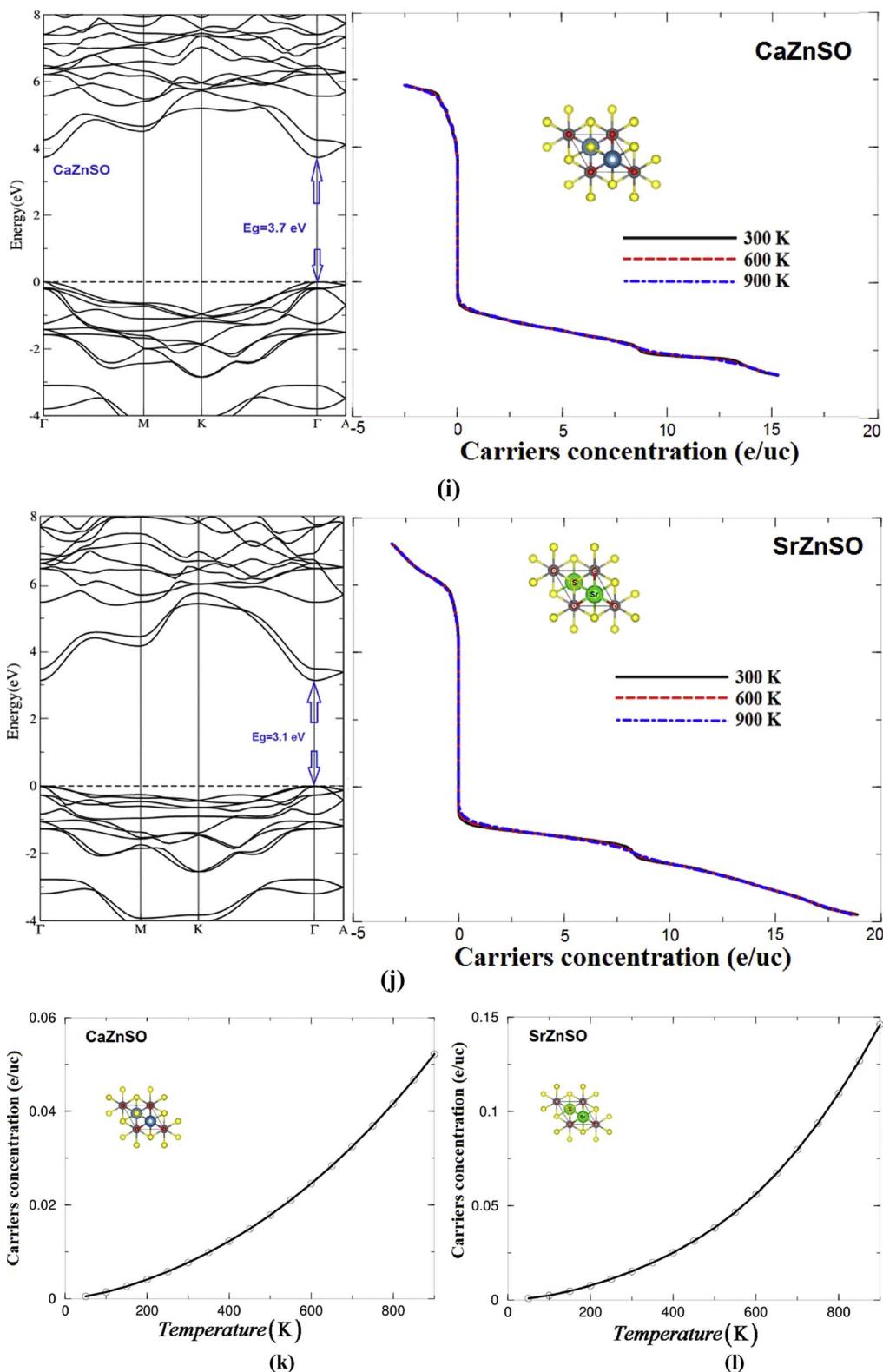
Fig. 3. (*continued*)

was noticed that from the electronic band structure (Fig. 2c), the high k-dispersion bands around Fermi level (E_F) possess low effective masses, and hence, high mobility carriers (Table 1), which favors the enhancement of the charge transfer process, and the effective mass provides essential information to understand the photocatalytic mechanism. The mobility of the photogenerated carriers significantly influences the photocatalytic efficiency [63,64]: the higher photogenerated carrier mobility favors the enhancement of the photocatalytic performance [65]. Furthermore, we calculated the effective mass difference ($D = m_e^*/m_h^*$) between e^- and h^+, as shown in Table 1 [66–69]. Recently, Li et al. [70] reported that the recombination of photogenerated electrons and holes is much faster than the transport from bulk to the surface reactive site and the catalytic reaction. Thus, in most cases, fast mobility favors the charge migration to the surface of

Table 1
Calculated effective masses.

Compound							
	m_e^*/m_o	m_{hh}^*/m_o	m_{lh}^*/m_o	$D = m_{hh}^*/m_e^*$	$D = m_e^*/m_{hh}^*$	$D = m_{lh}^*/m_e^*$	$D = m_e^*/m_{lh}^*$
CaZnSO	0.00852	0.04097	0.02437	4.80868	0.20795	2.86032	0.34961
SrZnSO	0.01031	0.03571	0.03709	3.46362	0.28871	3.59747	0.27797

the photocatalyst to participate in the reaction. In contrast, slow mobility of electrons and holes is more prone to result in charge recombination. It is clear from Table 1 that the effective mass of h^+ is bigger than that of e^-, resulting in a significant difference in the mobility between e^- and h^+; thus, we can deduce that the photogenerated carriers can transfer fast along different directions. The mobility of photoexcited carriers can be indirectly assessed by their effective mass ($\eta_e = e\tau_e/m_e^*$ and $\eta_h = e\tau_h/m_h^*$). The large mobility difference is useful to the separation of e^- and h^+, reduction of the e^- and h^+ recombination rate, and improvement of the photocatalytic activity.

The temperature-dependent electrical conductivity (σ/τ) is calculated at a certain value of chemical potential as illustrated in Fig. 3(c, d). It is clear that σ/τ increases with increasing the temperature (T). The rapid increase in σ/τ with increasing T is due to enhancing the charge carrier's concentration (n) and the mobility of the electrons in the conduction band. Fig. 3(e, f) shows the carrier's mobility as a function of n, which clearly shows a significant reduction in the carrier's mobility with an increase in the carrier's concentration due to increasing the scattering. To support this statement, we have investigated the carrier's mobility as a function of T, as shown in Fig. 3(g, h). It clearly shows a significant reduction in the carriers̍ mobility with an increase in T, which is attributed to the fact that raising T causes an increase in the vibration, and hence, the mobility, resulting in an increase in the scattering which leads to suppression of the mobility.

For further explanation of the semiconductor's 'photo-excitation' state mechanism in CaZnSO and SrZnSO, we calculated n as a function of chemical potential at three constant temperatures, as shown in Fig. 3(i, j), which clearly shows the negative electron (n-type conductions) and positive hole (p-type conductions) pair. The positive hole (h^+) breaks apart the water molecule to form hydrogen gas and a hydroxyl radical. Whereas the negative electron (e^-) reacts with the oxygen molecule to form a super-oxide anion. This cycle occurs continuously in the presence of the light. Furthermore, we investigated n as a function of T at fixed chemical potential, as shown in Fig. 3(k, l). It is clear that the n increases exponentially with increasing T and reveals that CaZnSO and SrZnSO are p-type semiconductors. To further understand the semiconductor's 'photo-excitation' state mechanism in CaZnSO and SrZnSO, the electronic band structure, the angular momentum character of various structures and the electronic charge density distribution are calculated so as to investigate the suitability of XZnSO to be used as active photocatalysts. The calculated electronic band structures (left panels of Fig. 3i, j)) reveal the band gap nature and the orbitals that form the top of the valence bands and the bottom of the conduction bands. It was found that CaZnSO (SrZnSO) possesses a direct band gap of about 3.7 (3.1) eV, and the Zn-3d/O-2p/S-3p antibonding crystal orbitals lying at the top of the valence band can readily accommodate holes generated. Therefore, CaZnSO and SrZnSO are p-type semiconductors. To gain deeper insight into the electronic structure, the total density of states and the angular momentum character of various structures are calculated and presented in Fig. 4(a–j). Fig. 4(a,b) explores the total density of states of each atom participating in the CaZnSO and SrZnSO structures. In order to visualize the contribution and the role of each orbital, the angular momentum character of (Ca-4s/3p) Sr-5s/4p/3d, Zn-4s/3p/3d, S-3s/3p and O-2s/2p orbitals are plotted, as shown in Fig. 4(c–j), which reveals the strong hybridization between the orbitals. It was noticed that there is a strong hybridization

between O-2s and (Ca-3p)Sr-4p, S-3p and O-2p, Zn-4s and Zn-3p, (Ca-4s) Sr-5s and Zn-4s/3p orbitals. The hybridization may lead to the formation of covalent bonding and the strength of the covalent bonding is related to the degree of the hybridization. We should emphasize that the covalent bonding is more favorable for the transport of the carriers than the ionic one [71].

To support this statement, the bond lengths, bond angles, charge transfer and electronic charge density distributions are investigated. To visualize the nature of the charge transfer and the chemical bonding, the electronic charge density distribution in (1 0 0) and (1 0 1) crystallographic planes are obtained, as shown in Fig. 5. Following the Pauling scale, the electronegativity of (Ca) Sr, Zn, S and O are (1.0) 0.95 < 1.65 < 2.58 < 3.44 [72,73], which indicates that the oxygen atom shows the highest electronegativity. This implies that an efficient charge transfer occurs towards S and O atoms which are surrounded by uniform spheres of charge density and the maximum charge accumulates around S and O atoms, as indicated by the blue color (Fig. 5). The blue color indicates the maximum charge intensity (1.0000) as shown by the thermo-scale (Fig. 5). The (1 0 0) crystallographic plane of CaZnSO clearly shows ZnS₃O tetrahedral in which the Zn-S bond is equal to 2.3712 Å, close to the experimental one [3]. For SrZnSO, the (1 0 0) crystallographic plane shows one face of the SrS₃O₃ octahedral in which the Sr-O bond is equal to 3.383 Å and the Sr-S = 3.181 Å, which is very close to the experimental values [2]. The (1 0 1) plane of CaZnSO (SrZnSO) shows both SrS₃O₃ octahedral and ZnS₃O tetrahedral where the Zn-O bond is equal to 1.899 (1.893) Å and Zn-S = 2.3712 (2.4169) Å, in close agreement with the experimental data [2,3]. It also shows that S and O atoms are surrounded by uniform spheres of charge density and the maximum charge accumulates around O and S atoms, as indicated by the blue color.

For a description of the character of the bonding, the difference of the electronegativity (X_A-X_B) is crucial [74], where X_A and X_B denote the electronegativity of the A and B atoms in general. With an increase in the difference, the ionic character (P) of the bonding increases. The percentage of P for the bonding can be obtained by following the relation [74]:

$$P(\%) = 16(X_A - X_B) + 3.5(X_A - X_B)^2 \tag{3}$$

The calculated values of P are given in Table 2. It is clear that the Zn atom in ZnS₃O tetrahedral in both compounds forms mostly covalent and partially ionic bonding with S and O atoms, see Table 2. Whereas in the CaS₄O₃ (SrS₄O₃) octahedral, the Ca (Sr) atoms form mostly covalent and partially ionic bonding with O atoms, and mostly ionic and partially covalent bonds with S (see Table 2). The crystallographic planes show that a charge transfer towards O and S atoms occurs, as is shown by the blue uniform spheres surrounding the O and S atoms indicating the maximum charge accumulated according to the thermo-scale (Fig. 4). To provide a comparison of quantities between theoretical and experimental values of the bond lengths and angles, we calculated the bond lengths and angles for the CaZnSO and SrZnSO single crystals, as shown in Table S3 and S4 (supplementary materials). It is clear that there is good agreement with the experimental data [2,3] and confirms that the Zn-O bond length is shorter than that of the Zn-S; also the Ca−O (Sr−O) bond length is shorter than that of the Ca−S (Sr−S). The three angles of O−Zn−S in the ZnS₃O tetrahedral are equal; the three S−Zn−S angles are also equal (Fig. 1), which reveals the symmetry of
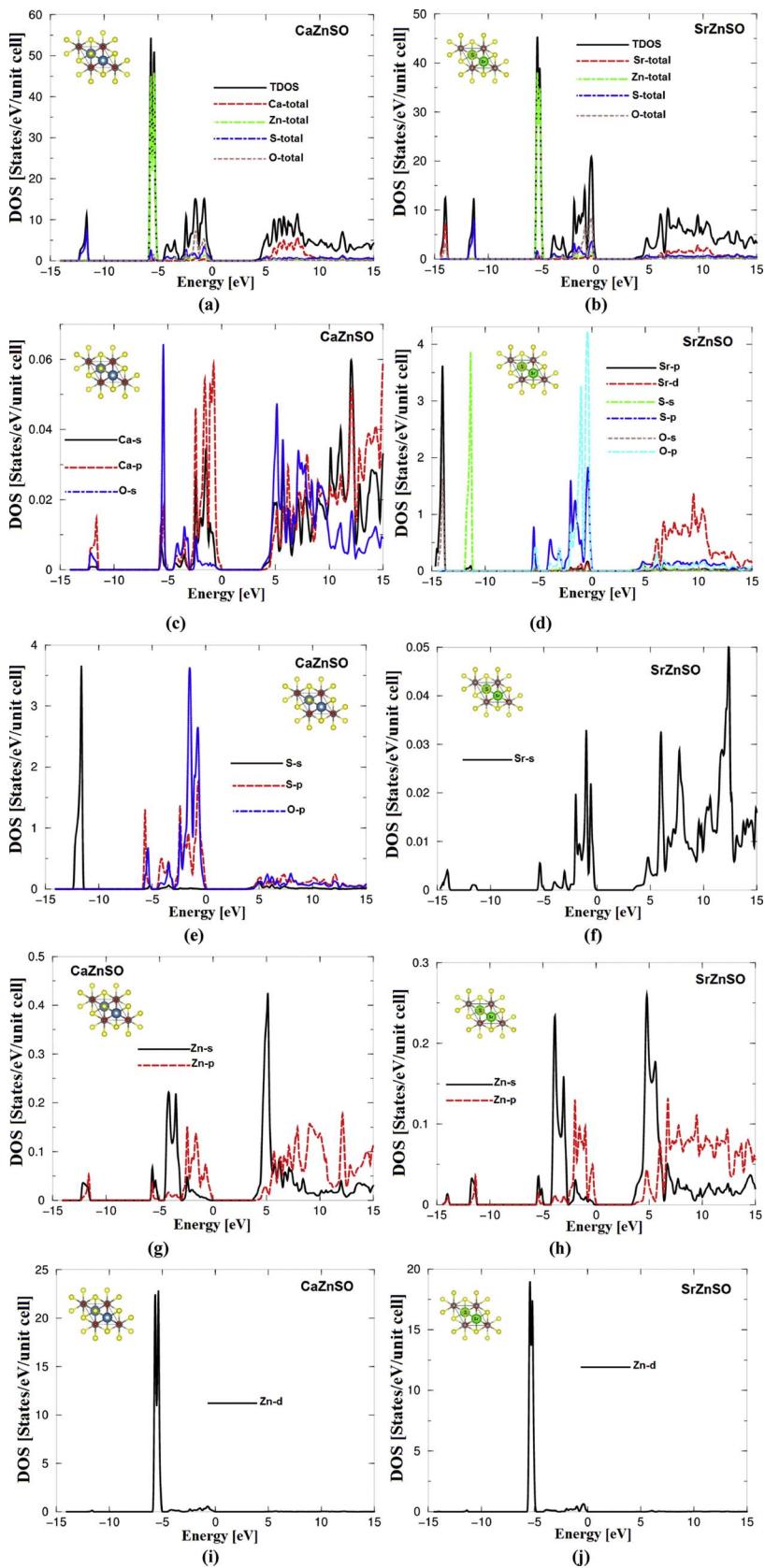
Fig. 4. (a–j) The projected density of states along with the angular momentum character of various structures.
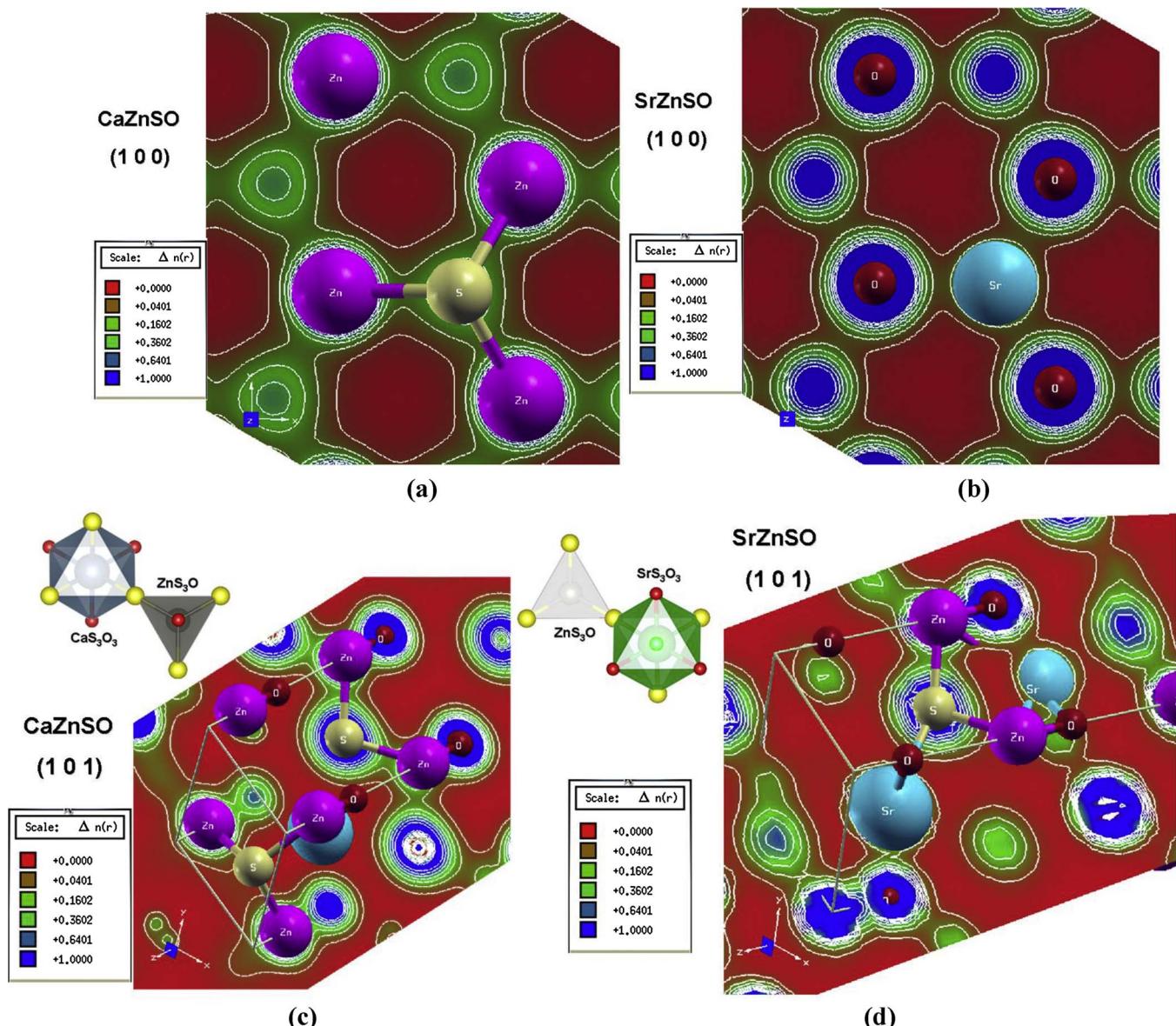
Fig. 5. (a–d) The charge density distribution of CaZnSO and SrZnSO in (100) and (101) crystallographic planes along with the thermoscale.

Table 2
The calculated values of the ionic character.

CaZnSO		SrZnSO	
Bonds	P(%)	Bonds	P(%)
Ca−O	59.87	Sr−O	61.54
Ca−S	34.01	Sr−S	35.37
Zn−O	39.85	Zn−O	39.85
Zn−S	17.90	Zn−S	17.90

the ZnS_3O tetrahedral in good agreement with the experimental data [2,3]. The bond lengths and the two crystallographic planes reveal that the XZnSO single crystals possess considerable anisotropy.

4. Conclusions

To investigate the suitability of CaZnSO and SrZnSO to be used as active photocatalysts, an *ab initio* calculation from first to second-principles calculations were performed utilizing the full-potential method and the BoltzTraP code. The photophysical, structure, and

photocatalytic and transport properties of the two newly synthesized sulfide oxides CaZnSO and SrZnSO were comprehensively investigated by means of first and second-principles calculation to explore the semiconductor's 'photo-excitation' state mechanism in these compounds. At the same time, we investigated the influence of the substitution of Ca^{2+} by Sr^{2+} on the structural properties, and hence, on the photocatalytic properties. The obtained photophysical properties show that the absorption edge moves from $\lambda = 387.4 \rightarrow \lambda = 442.7$ nm, which corresponds to the direct optical band gap of 3.2 eV → 2.8 eV, which is well matched with the solar spectrum and the sufficient negative conduction band potential for reduction of H^+/H_2. The calculated electronic band structure and the angular momentum character of various structures confirm that CaZnSO and SrZnSO possess a direct fundamental energy band gap of about 3.7 eV (CaZnSO) → 3.1 eV (SrZnSO), and the electronic charge distribution reveals a clear map of the electronic charge transfer and the chemical bonding. The carrier concentration (n) as a function of chemical potential at three constant temperatures (T) and n as a function of T at fixed chemical potential were calculated. Calculations show that n increases exponentially with increasing T and reveals that both CaZnSO and SrZnSO are p-type semiconductors. Thus, the non-centro-symmetric CaZnSO and SrZnSO

satisfied all requirements to be efficient photocatalysts. This will greatly improve the search efficiency and greatly help experiments aimed at saving resources in the exploration of new photocatalysts with good photocatalytic performance.

Author contribution

A.H. Reshak, as a professor with PhD in physics and PhD in materials engineering has performed the calculations, analyzing and discussing the results and writing the manuscript.

Competing financial interests

The author declare no competing financial interests.

Acknowledgments

Appendix A. Supplementary data

Supplementary data associated with this article can be found, in the online version, at https://doi.org/10.1016/j.apcatb.2017.12.006.

References

[1] Z.A. Gal, O.J. Rutt, C.F. Smura, T.P. Overton, N. Barrier, S.J. Clarke, J. Hadermann, Structural chemistry and metamagnetism of an homologous series of layered manganese oxysulfides, J. Am. Chem. Soc. 128 (2006) 8530.
[2] W. Liu, K.T. Lai, K. Eckhardt, Y. Prots, U. Burkhardt, M. Valldor, Synthesis and characterization of sulfide oxide SrZnSO with strongly polar crystal structure, J. Solid State Chem. 246 (2017) 225–229.
[3] T. Sambrook, C.F. Smura, S.J. Clarke, K.M. Ok, P.S. Halasyamani, Structure and physical properties of the polar oxysulfide CaZnOS, Inorg. Chem. 46 (2007) 2571–2574.
[4] S.F. Jin, Q. Huang, Z.P. Lin, Z.L. Li, X.Z. Wu, T.P. Ying, G. Wang, X.L. Chen, Two-dimensional magnetic correlations and partial long-range order in geometrically frustrated CaOFeS with triangle lattice of Fe ions, Phys. Rev. B 91 (2015) 094420.
[5] E.J.T. Salter, J.N. Blandy, S.J. Clarke, Crystal and magnetic structures of the oxide sulfides CaCoSO and BaCoSO, Inorg. Chem. 55 (2016) 1697–1701.
[6] B.W. Liu, X.M. Jiang, G.E. Wang, H.Y. Zeng, M.J. Zhang, S.F. Li, W.H. Guo, G.C. Guo, Oxychalcogenide BaGeOSe2. Highly distorted mixed-anion building units leading to a large second-harmonic generation response, Chem. Mater. 27 (2015) 8189–8192.
[7] H. Zhang, X. Chen, Z. Li, J. Kou, T. Yu, Z. Zou, Preparation of sensitized ZnS and its photocatalytic activity under visible light irradiation, J. Phys. D: Appl. Phys. 40 (2007) 6846–6849.
[8] G. Wang, B. Huang, Z. Li, Z. Lou, Z. Wang, Y. Dai, M.-H. Whangbo, Synthesis and characterization of ZnS with controlled amount of S vacancies for photocatalytic H2 production under visible light, Sci. Rep. 5 (2015) 8544, http://dx.doi.org/10.1038/srep08544.
[9] J.-S. Hu, L.-L. Ren, Y.-G. Guo, H.-P. Liang, A.-M. Cao, L.-J. Wan, C.-L. Bai, Mass production and high photocatalytic activity of ZnS nanoporous nanoparticles, Angew. Chem. 117 (2005) 1295–1299.
[10] G.-L. Lee, J.J. Wu, Recent developments in ZnS photocatalysts from synthesis to photocatalytic applications — A review, Powder Technol. 318 (2017) 8–22.
[11] M. Sharma, T. Jain, S. Singh, O.P. Pandey, Photocatalytic degradation of organic dyes under UV–Visible light using capped ZnS nanoparticles, Sol. Energy 86 (2012) 626–633.
[12] R.Y. Hong, J.H. Li, L.L. Chen, D.Q. Liu, H.Z. Li, Y. Zheng, J. Ding, Synthesis, surface modification and photocatalytic property of ZnO nanoparticles, Powder Technol. 189 (2009) 426–432.
[13] K.M. Lee, C.W. Lai, K.S. Ngai, J.C. Juan, Recent developments of zinc oxide based photocatalyst in water treatment technology: a review, Water Res. 88 (2016) 428–448.
[14] C. Gionco, D. Fabbri, P. Calza, M.C. Paganini, Synthesis, characterization, and photocatalytic tests of N-doped zinc oxide: a new interesting photocatalyst, hindawi publishing corporation, J. Nanomater. (2016) 4129864 https://doi.org/10.1155/2016/4129864.
[15] X. Chen, Z. Wu, D. Liu, Z. Gao, Preparation of ZnO photocatalyst for the efficient and rapid photocatalytic degradation of azo dyes, Chen et al, Nanoscale Res. Lett. 12 (2017) 143, http://dx.doi.org/10.1186/s11671-017-1904-4.
[16] W. Raza, S.M. Faisal, M. Owais, D. Bahnemann, M. Muneer, Facile fabrication of highly efficient modified ZnO photocatalyst with enhanced photocatalytic, antibacterial and anticancer activity, RSC Adv. 6 (2016) 78335.
[17] R.J. Barnes, R. Molina, J. Xu, P.J. Dobson, I.P. Thompson, Comparison of TiO2 and ZnO nanoparticles for photocatalytic degradation of methylene blue and the correlated inactivation of gram-positive and gram-negative bacteria, J. Nanopart. Res. 15 (2013) 1432, http://dx.doi.org/10.1007/s11051-013-1432-9.
[18] M.I. Kolinko, I.V. Kityk, A.S. Krochuk, Band energy parameters and density functions of orthorhombic TlI, J. Phys. Chem. Solids 53 (1992) 1315–1320.
[19] G.E. Davydyuk, O.Y. Khyzhun, A.H. Reshak, H. Kamarudin, G.L. Myronchuk, S.P. Danylchuk, A.O. Fedorchuk, L.V. Piskach, M. Mozolyuk Yu, O.V. Parasyuk, Photoelectrical properties and the electronic structure of tl1-xIn1-xSnxSe2 (x = 0, 0. 1, 0. 2, 0. 25) single crystalline alloys, Phys. Chem. Chem. Phys. 15 (2013) 6965.
[20] A.H. Reshak, Y.M. Kogut, A.O. Fedorchuk, O.V. Zamuruyeva, G.L. Myronchuk, O.V. Parasyuk, H. Kamarudin, S. Auluck, K.L. Plucinskig, J. Bila, Linear, non-linear optical susceptibilities and the hyperpolarizability of the mixed crystals Ag0.5Pb1.75Ge(S1-xSex)4: experiment and theory, Phys. Chem. Chem. Phys. 15 (2013) 18979.
[21] V.V. Atuchin, T.A. Gavrilova, J.-C. Grivel, V.G. Kesler, Electronic structure of layered titanate Nd2Ti2O7, Surf. Sci. 602 (2008) 3095–3099.
[22] V.V. Atuchin, T.A. Gavrilova, J.-C. Grivel, V.G. Kesler, Electronic structure of layered ferroelectric high-k titanate La2Ti2O7, J. Phys. D: Appl. Phys. 42 (2009) 035305.
[23] O.Y. Khyzhun, V.L. Bekenev, V.V. Atuchin, E.N. Galashov, V.N. Shlegel, Electronic properties of ZnWO4 based on ab initio FP-LAPW band-structure calculations and X-ray spectroscopy data, Mater. Chem. Phys. 140 (2013) 558–595.
[24] V.V. Atuchin, E.N. Galashov, O.Y. Khyzhun, V.L. Bekenev, L.D. Pokrovsky, A.Yu. Borovlev, V.N. Zhdankov, Low Thermal Gradient Czochralski grow thoflarge CdWO4 crystals and electronic properties of (010) cleaved surface, J. Solid State Chem. 236 (2016) 24–31.
[25] K. Nouneh, A.H. Reshak, S. Auluck, I.V. Kityk, R. Viennois, S. Benet, S. Charar, Band energy and thermoelectricity of filled skutterudites LaFe4Sb12 and CeFe4Sb12, J. Alloys Compd. 437 (2007) 39–46.
[26] A.H. Reshak, K. Nouneh, I.V. Kityk, J. Bila, S. Auluck, H. Kamarudin, Z. Sekkat, Structural, Electronic and optical properties in earth-abundant photovoltaic absorber of Cu2ZnSnS4 and Cu2ZnSnSe4 from DFT calculations, Int. J. Electrochem. Sci. 9 (2014) 955–974.
[27] H. Huang, Y. He, X. Li, M. Li, C. Zeng, F. Dong, X. Du, T. Zhangd, Y. Zhang, Bi2O2(OH)(NO3) as a desirable [Bi2O2]2+ layered photocatalyst: strong intrinsic polarity, rational band structure and {001} active facets co-beneficial for robust photooxidation capability, J. Mater. Chem. A 3 (2015) 24547–24556.
[28] H. Huang, Y. He, Z. Lin, L. Kang, Y. Zhang, Two novel Bi-based borate photocatalysts: crystal structure, electronic structure, photoelectrochemical properties, and photocatalytic activity under simulated solar light irradiation, J. Phys. Chem. C 117 (2013) 22986–22994.
[29] J. Zhang, W. Yu, J. Liu, B. Liud, Illustration of high-active Ag2CrO4 photocatalyst from the first-principle calculation of electronic structures and carrier effective mass, Appl. Surf. Sci. 358 (2015) 457–462.
[30] X. Li, J. Zhao, J. Yang, Semihydrogenated BN sheet: a promising visible-light driven photocatalyst for water splitting, Sci. Rep. 3 (2013) 1858.
[31] D.W. Hwang, J.S. Lee, W. Li, Oh Se Hyuk, Electronic band structure and photocatalytic activity of Ln2Ti2O7 (Ln = La, Pr, Nd), J. Phys. Chem. B 107 (2003) 4963–4970.
[32] H. Huang, X. Li, J. Wang, F. Dong, P.K. Chu, T. Zhang, Y. Zhang, Anionic group self-doping as a promising strategy: band-gap engineering and multi-functional applications of high-performance CO32–doped Bi2O2CO3, ACS Catal. 5 (2015) 4094–4103.
[33] H. Huang, X. Han, X. Li, S. Wang, P.K. Chu, Y. Zhang, Fabrication of multiple heterojunctions with tunable visible-light-active photocatalytic reactivity in BiOBr–BiOI full-range composites based on microstructure modulation and band structures, ACS Appl. Mater. Interfaces 7 (2015) 482–492.
[34] (a) C. Liu, Y. Zhang, F. Dong, A.H. Reshak, L. Ye, N. Pinna, C. Zeng, T. Zhang, H. Huang, Chlorine intercalation in graphitic carbon nitride for efficient photocatalysis, Appl. Catal. B: Environ. 203 (2017) 465–474;
(b) H. Huang, S. Tu, C. Zeng, T. Zhang, A.H. Reshak, Y. Zhang, Macroscopic polarization enhancement promoting photo- and piezoelectric-induced charge separation and molecular oxygen activation, Angew. Chem. Int. Ed. (2017), http://dx.doi.org/10.1002/anie.201706549.
[35] A.H. Reshak, Quantum dots in photocatalytic applications: efficiently enhancing visible light photocatalytic activity by integrating CdO quantum dots as sensitizer, Phys. Chem. Chem. Phys. 19 (2017) 24915.
[36] (a) A.H. Reshak, Photocatalytic water splitting solar-to-hydrogen energy conversion: perovskite-type hydride XBeH3 (X = Li or Na) as active photocatalysts, J. Catal. 351 (2017) 119–129;
(b) A.H. Reshak, Photophysical, transport and structure properties of Tl10Hg3Cl16 single crystals: Novel photocatalytic water-splitting solar-to-hydrogen energy conversion, J. Catal. 352 (2017) 142–154;
(c) A.H. Reshak, Active Photocatalytic Water Splitting Solar-to-Hydrogen Energy Conversion: Chalcogenide Photocatalyst Ba2ZnSe3 under Visible Irradiation, Appl. Catal. B: Environ. 221 (2018) 17–26.
[37] A.H. Reshak, S. Auluck, Photocatalytic water-splitting solar-to-hydrogen energy conversion: novel LiMoO3(IO3) molybdenyl iodate based on WO3-type sheets, J.

Catal. 351 (2017) 1–9.

[38] P. Blaha, K. Schwarz, G.K.H. Madsen, D. Kvasnicka, J. Luitz, WIEN2k, An Augmented Plane Wave Plus Local Orbitals Program for Calculating Crystal Properties, Vienna University of Technology, Austria, 2001.

[39] J.P. Perdew, S. Burke, M. Ernzerhof, Generalized gradient approximation made simple, Phys. Rev. Lett. 77 (1996) 3865.

[40] F. Tran, P. Blaha, Accurate band gaps of semiconductors and insulators with a semilocal exchange-correlation potential, Phys. Rev. Lett. 102 (2009) 226401.

[41] P.B. Allen, J.R. Chelikowsky, S.G. Louie (Eds.), Quantum Theory of Real Materials, Kluwer, Boston, 1996, pp. 219–250.

[42] J.M. Ziman, Electrons and Phonons, Clarendon, Oxford, 2001.

[43] C.M. Hurd, The Hall Effect in Metals and Alloys, Plenum, New York, 1972.

[44] G.K.H. Madsen, D.J. Singh, BoltzTraP: A code for calculating band-structure dependent quantities, Comput. Phys. Commun. 175 (2006) 67–71.

[45] P.E. Blöchl, O. Jepsen, O.K. Andersen, Improved tetrahedron method for Brillouin-zone integrations, Phys. Rev. B Condens. Matter. 15 (1994) 16223.

[46] T. Goldacker, V. Abetz, R. Stadler, I. Erukhimovich, L. Leibler, Non-centrosymmetric superlattices in block copolymer blends, Nature 398 (1999) 137–139.

[47] M. Stock, S. Dunn, Influence of the ferroelectric nature of lithium niobate to drive photocatalytic dye decolorization under artificial solar light, J. Phys. Chem. C 116 (2012) 20854–20859.

[48] Y. Cui, J. Briscoe, S. Dunn, Effect of ferroelectricity on solar-light-driven photocatalytic activity of BaTiO3—Influence on the carrier separation and stern layer formation, Chem. Mater. 25 (2013) 4215-42-23.

[49] S.V. Kalinin, D.A. Bonnell, Nanoscale Phenomena in Ferroelectric Thin Films, Kluwer Academic Publications, Dordrecht The Netherlands, 2004, pp. 182–216.

[50] S. Dunn, P.M. Jones, D.E. Gallardo, Photochemical growth of silver nanoparticles on c- and c+ domains on lead zirconate titanate thin films, J. Am. Chem. Soc. 129 (2007) 8724–8728.

[51] Y. Inoue, K. Sate, K. Sato, H. Miyama, Photoassisted water decomposition by ferroelectric lead zirconate titanate ceramics with anomalous photovoltaic effects, J. Phys. Chem. 90 (1986) 2809.

[52] M.T. Buelow, A.J. Gellman, The transition state for metal-catalyzed dehalogenation: CI bond cleavage on Ag(111), J. Am. Chem. Soc. 123 (2001) 1440.

[53] X.C. Wang, et al., Nat. Mater. 8 (2009) 76–80.

[54] Jinfeng Zhang, Weilai Yu, Jianjun Liu, Baoshun Liu, Appl. Surf. Sci. 358 (2015) 457–462.

[55] M. Matsumura, S. Furukawa, Y. Saho, H. Tsubomura, Cadmium sulfide photocatalyzed hydrogen production from aqueous solutions of sulfite: effect of crystal structure and preparation method of the catalyst, J. Phys. Chem. 89 (1985) 1327–1329.

[56] S.W. Liu, J.G. Yu, M. Jaroniec, Tunable photocatalytic selectivity of hollow TiO2 microspheres composed of anatase polyhedra with exposed {001} facets, J. Am. Chem. Soc. 132 (2010) 11914–11916.

[57] J.R. Ran, J.G. Yu, M. Jaroniec, Ni(OH)2 modified CdS nanorods for highly efficient visible-light-driven photocatalytic H2 generation, Green Chem. 13 (2011) 2708–2713.

[58] J.C. Wu, J.W. Zheng, P. Wu, R. Xu, J. Phys. Chem. C 115 (2011) 5675–5682.

[59] S. Banerjee, J. Gopal, P. Muraleedharan, A.K. Tyagi, B. Raj, Curr. Sci. 90 (2006) 1378–1383.

[60] P.J. Zhou, G. Yu, M. Jaroniec, All-solid-state Z-scheme photocatalytic systems, Adv. Mater. 26 (2014) 4920–4935.

[61] Q. Li, H. Meng, P. Zhou, Y.Q. Zheng, J. Wang, J.G. Yu, J.R. Gong, Zn1−xCdxS solid solutions with controlled bandgap and enhanced visible-light photocatalytic H2-production activity, ACS Catal. 3 (2013) 882–889.

[62] M.S. Dresselhaus, Solid State Physics Part II Optical Properties of Solids vol. 6, (2001).

[63] J.W. Tang, J.H. Ye, Photocatalytic and photophysical properties of visible-light-driven photocatalyst ZnBi12O20, Chem. Phys. Lett. 410 (2005) 104–107.

[64] T.L. Bahers, M.R. Rat, P. Sautet, Semiconductors used in photovoltaic and photocatalytic devices: assessing fundamental properties from DFT, J. Phys. Chem. C 118 (2014) 5997–6008.

[65] J. Sato, H. Kobayashi, Y. Inoue, Photocatalytic activity for water decomposition of indates with octahedrally coordinated d10 configuration II. Roles of geometric and electronic structures, J. Phys. Chem. B 107 (2003) 7970–7975.

[66] H.J. Zhang, L. Liu, Z. Zhou, Towards better photocatalysts: first-principles studies of the alloying effects on the photocatalytic activities of bismuth oxyhalides under visible light, Phys. Chem. Chem. Phys. 14 (2012) 1286–1292.

[67] J.F. Zhang, P. Zhou, J.J. Liu, J.G. Yu, New understanding of the difference of photocatalytic activity among anatase, rutile and brookite TiO2, Phys. Chem. Chem. Phys. 16 (2014) 20382–20386.

[68] J. Zhang, W. Yu, J. Liu, B. Liu, Illustration of high-active Ag2CrO4 photocatalyst from the first-principle calculation of electronic structures and carrier effective mass, Appl. Surf. Sci. 358 (2015) 457–462.

[69] J. Yang, P. Jiang, M. Yue, D. Yang, R. Cong, W. Gao, T. Yang, Bi2Ga4O9: an undoped single-phase photocatalyst for overall water splitting under visible light, J. Catal. 345 (2017) 236–244.

[70] J. Li, L. Cai, J. Shang, Y. Yu, L. Zhang, Giant enhancement of internal electric field boosting bulk charge separation for photocatalysis, Adv. Mater. 28 (2016) 4059–4064.

[71] F. Wu, H.Z. Song, J.F. Jia, X. Hu, Effects of Ce, Y, and Sm doping on the thermoelectric properties ofBi2Te3 alloy, Progress Nat. Sci.: Materials. Int. 23 (2013) 408–412.

[72] https://en.wikipedia.org/wiki/Electronegativity.

[73] https://en.wikipedia.org/wiki/Template:Periodic_table_ (electronegativity_by_ Pauling_scale).

[74] Schlusseltechnologien Key Technologies, 41st IFF Springschool, 2010, pp A1-18.